Alignment-assisted high thermal conductivity and thermal anisotropy in poly(methyl methacrylate)/graphene nanolaminates

Bohai Liu,[1] Christos Pavlou,[2,3] Meguya Ryu,[4,5] Ayumi Ishihara,[6] Jizhu Hu,[1,7] Costas Galiotis,[2,3,*] Junko Morikawa,[5,8,†] Xiangfan Xu,[1,‡] and George Fytas[7,§]

[1] *Center for Phononics and Thermal Energy Science, School of Physics Science and Engineering, Tongji University, 200092 Shanghai, PR China*

[2] *Institute of Chemical Engineering Sciences, Foundation of Research and Technology-Hellas (FORTH/ICE-HT), Stadiou Street, 26504 Platani, Patras, Greece*

[3] *Department of Chemical Engineering, University of Patras, 26504 Patras, Greece*

[4] *National Metrology Institute of Japan (NMIJ), National Institute of Advanced Industrial Science and Technology (AIST), Tsukuba 305-8563, Japan*

[5] *School of Materials and Chemical Technology, Institute of Science Tokyo, Ookayama, Meguro-ku, Tokyo 152-8550, Japan*

[6] *2nd Business Department, Quantum Design Japan Incorporated, Tokyo 171-0042, Japan*

[7] *Max Planck Institute for Polymer Research, Ackermannweg 10, 55128 Mainz, Germany*

[8] *Research Center for Autonomous Systems Materialogy (ASMat), Institute of Innovative Research, Institute of Science Tokyo, 4259 Nagatsuta-cho, Midori-ku, Yokohama, Kanagawa, 226-8501, Japan*

(Received 17 November 2024; revised 22 April 2025; accepted 30 June 2025; published 30 July 2025)

Understanding heat transport at the graphene-polymer (Gr-polymer) interface is the key to improve the thermal conductivity of Gr-based nanocomposites. Here, we fabricate poly (methyl methacrylate)/graphene (PMMA/Gr) nanolaminates and find an ultrahigh increase of the in-plane thermal conductivity ($8.9 \pm 0.9\,\mathrm{Wm^{-1}K^{-1}}$) compared to net PMMA and the thermal conductivity anisotropy (approximately equal to 53) at low Gr loading (1 vol. %). The strong anisotropic thermal conduction can be attributed to the predominantly in-plane oriented Gr nanoflake and, intriguingly, the graphene-induced planar alignment of PMMA in the proximity of Gr, as revealed by polarized infrared spectroscopic (p-IR) imaging, nano-FTIR and IR s-SNOM. We demonstrated the contribution of interface-induced confinement to the observed thermal property, providing deeper insights into heat transport at the Gr-polymer interface.

DOI: 10.1103/5zfl-986l

I. INTRODUCTION

High thermally anisotropic polymer nanocomposites are useful in modern electronics, as they enable the undesired heat to dissipate in one direction while keeping the device thermally and electrically isolated [1–3]. As a canonical example, graphene-based (Gr-based) composites have attracted enormous attention due to Gr's superhigh in-plane thermal conductivity $\kappa_{\mathrm{Gr},\parallel}$ [4] and thermal anisotropy [5,6]. However, achieving high thermal conductivity and anisotropy in these composites remains a significant challenge. Major limitations include the inherently reduced thermal conductivity of encapsulated Gr [due to the suppressed out-of-plane acoustic (ZA) phonon mode], the poor contact and the large interfacial thermal resistance (ITR) between Gr and polymer, with the latter being the dominant factor that limits thermal performance [5,6].

The mechanisms of heat transport at the Gr-polymer interface are yet to be fully understood [7]. The acoustic mismatch model (AMM) and the diffuse mismatch model (DMM) were initially proposed to estimate the ITR between the liquid-solid and solid-solid interface, which fail to accurately estimate the ITR in nanocomposites without any atomic-level description of phonon scattering [8]. Although molecular dynamics (MD) simulations have investigated the effects of bonding or adhesion strength between the filler and polymer matrix [9,10], they neglect the impact of other critical factors, such as interfacial

*Contact author: c.galiotis@iceht.forth.gr
†Contact author: morikawa.j.4f50@m.isct.ac.jp
‡Contact author: xuxiangfan@tongji.edu.cn
§Contact author: fytas@mpip-mainz.mpg.de

voids and the molecular alignment at the interface [5]. Recent studies show the thermal conductivity of polymers is highly dependent on their morphology; aligned polymer chains enable more effective heat transport along the covalent backbones [11–13]. Therefore, the knowledge of polymer conformation at the Gr-polymer interface is crucial for understanding heat transport in Gr/polymer nanocomposites. However, experiments of polymer conformations near the interface and their impact on thermal conductivity remain scarce.

In this work, the extreme confinement of the polymer is realized on a detectable scale in PMMA/Gr nanolaminates through the lift-off/float-on-wet transfer technique [14] with Gr volume fraction varies from 0.02% to 1%. The nanolaminates exhibit large enhancement of $\kappa_{\parallel}$, along with the high thermal conductivity anisotropy $\kappa_{\parallel}/\kappa_{\perp}$ at low Gr loading (1%). The sublinear dependence of $\kappa_{\parallel}$ and $\kappa_{\perp}$ on Gr loadings suggests the formation of oriented PMMA sublayers in the PMMA/Gr interfacial region, which is further confirmed by polarized infrared spectroscopic (*p*-IR) imaging and near-field FTIR. Our findings reveal that graphene can serve as a two-dimensional orientation template for PMMA chains, thereby enhancing the thermal conductivity of the nanocomposite.

II. RESULTS

A. Nanolaminate processing

PMMA/Gr nanolaminates were fabricated by implementing the semiautomatic iterative lift off and float on combined with the wet-deposition technique [14,15]. The atomic force microscope (AFM) image of CVD Gr on a Cu substrate shown in Fig. 1(a) indicates a relatively low wrinkle height (approximately 6 nm). The CVD graphene also exhibits large grain sizes (>90 μm) [14]. The samples are labeled as PMMA/$Gr_{\phi Gr}$, where ϕ_{Gr} denotes the per cent volume fraction of Gr. The total thicknesses of the samples as well as the correlation of the Gr volume fraction with the thickness of each PMMA layer are listed in Table S1 within the Supplemental Material. UV-vis-NIR and Raman techniques are utilized to characterize the quality of PMMA/Gr nanolaminates. Figure 1(b) shows representative UV-vis-NIR transmittance spectra of $(PMMA/Gr)_n$, where n denotes the number of Gr layers. The corresponding transmittance should amount to 87.0%, 49.8%, and 31.2% for repeating cycles $n = 6$, 30, and 50, respectively, since visible light absorption of Gr is 2.3% [16]. The experimental transmittance shows consistency with the computed values, indicating each Gr layer remains almost intact during the wet-transfer process. Raman spectra in Fig. 1(c) shows the intensity ratio of the *D* peak to *G* peak, $I(D)/I(G) \sim 0.17$, indicating almost negligible defects in Gr fillers [17]. Meanwhile, as a previous study [18] suggests, the nearly unchangeable peak positions for multiple stacking [black dashed lines in Fig. 1(c)] indicate that no residual stresses are developed in the nanolaminates after the fabrication process. These characterizations demonstrate the high quality of the PMMA/Gr nanolaminates, which is a prerequisite for high thermal conduction materials.

B. Thermal conductivity

The in-plane thermal conductivity, $\kappa_{\parallel}$, is shown in Fig. 2(a) as a function of Gr volume fraction, suggesting sublinear dependence. The experimental details could be found in Ref. [15]. The thermal conductivity of PMMA/Gr reaches $\kappa_{\parallel} = 8.9 \pm 0.9$ W m^{-1} K^{-1} notably at a relatively low (1%) Gr loading. To the best of our knowledge, this enhancement in the thermal conductivity is among

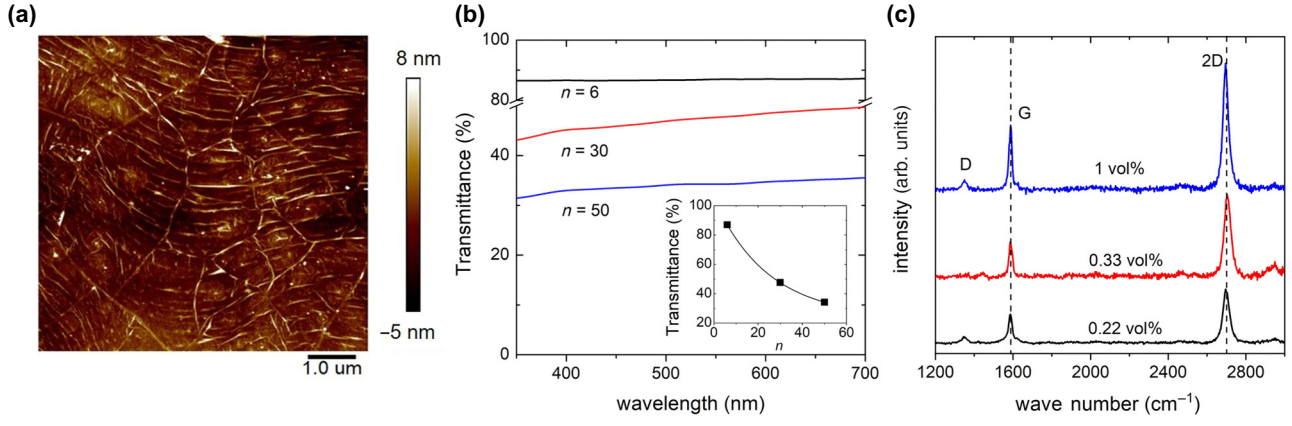

FIG. 1. Sample characterization. (a) An AFM image of the CVD Gr on the copper substrate, revealing large grains. (b) UV-vis transmittance spectra of $(PMMA/Gr)_n$ with different numbers of stacking cycles, n. Inset: UV-vis transmittance of $(PMMA/Gr)_n$ nanolaminates under a wavelength of 550 nm. (c) Representative Raman spectra of three PMMA/Gr nanolaminates with different Gr volume fraction. The black dash lines manifest the nearly unchangeable 2D and G peaks after the transfer process.

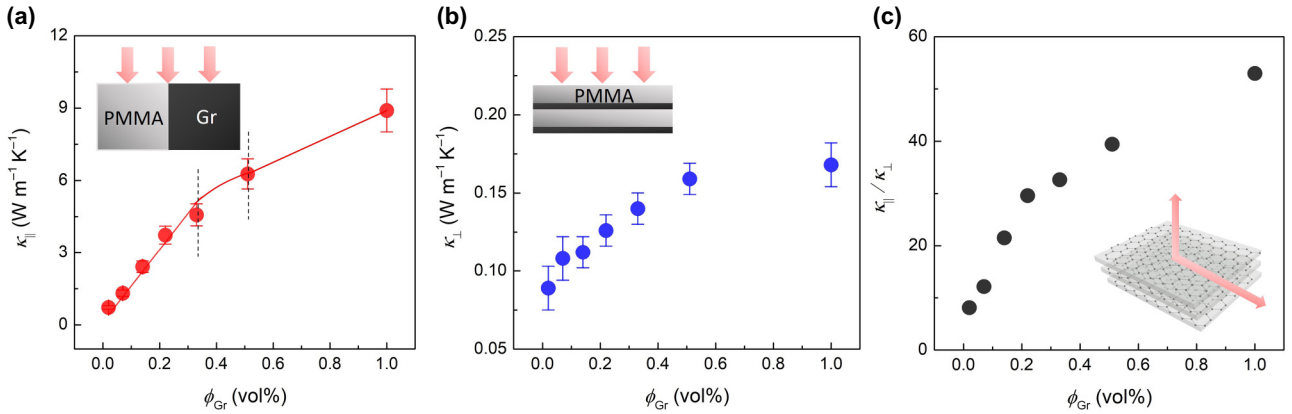

FIG. 2. Anisotropic heat conduction. (a) In-plane thermal conductivity of PMMA/Gr nanolaminates. Inset: thermal pathways in in-plane direction. The drawing of a solid line assumes a thickness dependent κ_{PMMA} on the premise of linear $\kappa_{\parallel}$ as a function of ϕ_{Gr}. (b) Cross-plane thermal conductivity of PMMA/Gr nanolaminates. Inset: thermal pathways in the cross-plane direction. (c) Anisotropy of thermal conductivity, $\kappa_{\parallel}/\kappa_{\perp}$, as a function of ϕ_{Gr}. Inset: a scheme of PMMA/Gr nanolaminates and the thermal transport in two directions.

one of the highest values reported for Gr or Gr-related polymer composites in this range of volumetric fraction [6,15,19]. A similar asymptotic behavior as in Fig. 2(b) with an increase of $\kappa_{\perp}$ from 0.089 ± 0.014 W m^{-1} K^{-1} to 0.17 ± 0.014 W m^{-1} K^{-1} with ϕ_{Gr}. The thermal conductivity anisotropy, $\kappa_{\parallel}/\kappa_{\perp}$, increases with ϕ_{Gr}, and reaches 53 at 1 vol. % Gr [Fig. 2(c)].

The parallel thermal transport model is usually applied to represent $\kappa_{\parallel}$ (ϕ_{Gr}) in nanolaminates, as schematically presented in the inset to Fig. 2(a): $\kappa_{\parallel} = (1-\phi_{Gr})\,\kappa_{PMMA} + \phi_{Gr}\,\kappa_{Gr,\parallel}$, where κ_{PMMA} and $\kappa_{Gr,\parallel}$ are the thermal conductivity of PMMA and Gr (in-plane), respectively. Constant values of κ_{PMMA} and $\kappa_{Gr,\parallel}$ would lead to a linear dependent $\kappa_{\parallel}$ (ϕ_{Gr}), in contrast to the nonlinear dependence in Fig. 2(a). The initial linear dependence for $\phi_{Gr} \leq 0.34\%$ is represented by $\kappa_{PMMA} = 0.1$ W m^{-1} K^{-1} and would yield an anomalous high value for supported Gr [20,21], $\kappa_{Gr,\parallel} = 1500$ W m^{-1} K^{-1}, which, in addition, fails to predict $\kappa_{\parallel}$ (ϕ_{Gr}) at higher ϕ_{Gr}. In the same context, the increase of the cross plane $\kappa_{\perp}$ with ϕ_{Gr} in Fig. 2(b) is also unexpected. Along this direction, the heat is being transported through three phases, Gr, Gr-PMMA interface, and PMMA until approaching the sensor. The anticipated series-model [scheme in Fig. 2(b) inset] reads $1/\kappa_{\perp} = \phi_{Gr}/\kappa_{Gr,\perp} + (1-\phi_{Gr})/\kappa_{PMMA} + \phi_{Gr}/(G_b h_{Gr})$. h_{Gr} (=0.34 nm) is the thickness of a single Gr layer and G_b is the thermal boundary conductance between Gr and PMMA. G_b is taken on the order of 10^9 W m^{-2} K^{-1}, similar to that in carbon nanotube and the PMMA interface [22]. In this case, $\kappa_{\perp}$ should decrease due to the increasing interfaces, in contrast to the observed trend in Fig. 2(b). One possible reason for the increased $\kappa_{\perp}$ with ϕ_{Gr} may relate to the wrinkled graphene, as shown in Fig. 1(a) [the effect of wrinkled graphene on $\kappa_{\perp}(\phi_{Gr})$ is addressed later]. Nevertheless, $\kappa_{\perp}(\phi_{Gr})$ should not keep increase with ϕ_{Gr} and therefore we are left to conclude that the assumption of a constant κ_{PMMA} in the series models might be invalid.

Overall, in-plane and cross-plane thermal transport should comply, respectively, with the parallel and series model, as the thermal pathways are, respectively, parallel and perpendicular to Gr layers. On the premise of a linear $\kappa_{\parallel}$ (ϕ_{Gr}) function over the full dilute ϕ_G regime and a robust $\kappa_{\perp}$ (ϕ_{Gr}) over the same ϕ_{Gr} range, it is probably incorrect, to assume $\kappa_{PMMA} = 0.1$ W m^{-1} K^{-1} in the representation of the experimental heat conductivity of Figs. 2(a) and 2(b). We note that if there is any effect in thermal conductivity because of the orientation of graphene itself with such low Gr loadings, thermal conductivity should decrease with Gr loading due to interfacial thermal resistance between Gr and PMMA in the cross-plane direction, and increase linearly in in-plane direction, in sharp contrast to the sublinear trend in both directions as we observed.

Atomistic simulations show that polymer chains can align on a graphite substrate [23], and more specifically, PMMA chains can orient near the Gr surface with a thickness of several nanometers [24,25]. It is known that thermal transport in polymers is highly related to the chain conformation [11,12]: the weak interchain hopping between entangled polymer chains in amorphous bulk polymers severely hampers heat transport [26]. Oriented polymers display enhanced thermal conductivity, as heat preferentially transports along the chains and the interchain hopping becomes suppressed [13]. We, therefore, postulate that PMMA orientation near the PMMA-Gr interface may underpin the unexpected $\kappa_{\parallel}$ and $\kappa_{\perp}$.

C. Planner alignment of PMMA

We employed the four-polarization method of Fourier transform infrared spectroscopic (p-IR) imaging, nano-FTIR, and infrared scattering scanning near-field

optical microscopy (IR s-SNOM) [27–29] to probe the PMMA chain conformation. The 4p-IR spectrum was recorded with incident light at four different polarization angles enabling the reconstruction of the arbitral in-plane orientation of the specific dipole. This method can simultaneously visualize the chemical information and orientation distribution [30]. An exemplary p-IR spectrum for PMMA/$Gr_{1\%}$ is presented in Fig. 3(a), with the C—O—C stretching band at 1242 cm^{-1}. We focus on this band because it is more amenable to the polymer chain orientation and is relevant to Gr-PMMA interactions [31]. Details of peaks at other frequencies can be found elsewhere [32]. The distribution orientation azimuth (ψ) of the PMMA chain estimated from p-IR measurement is shown in Fig. 3(b) as white arrows superimposed to the distribution of p-IR absorption at 1242 cm^{-1}. The cross section of the PMMA/Gr film was embedded in epoxy matrix, and the film cross section [bordered by red line in Fig. 3(b)] is oriented along $\psi = 124°$ direction. The Hermans orientation function $f_{ave} = 0.031$ [15], calculated from the absorbance, indicates the overall in-plane orientation of the PMMA [15,30]. As the spatial resolution of p-IR imaging is limited by the diffraction limit, the image pixel size was effectively 6.25 μm.

Nanoscale analysis was further performed by nano-FTIR with broadband illumination and IR s-SNOM combined with a quantum cascade laser (QCL). The Pt/Ir coated AFM cantilever was mechanically modulated and irradiated by broadband illumination/QCL. The scattered light was modulated, and its phase and amplitude were analyzed to determine the optical properties under the tip. The imaginary part of the scattered electromagnetic field relates to the absorption of the sample surface. Therefore, the absorption of nano-FTIR and IR s-SNOM can be defined as, $a = \mathrm{Im}[\sigma]$. The distribution of a at 1145 cm^{-1} from the cross section of PMMA/$Gr_{0.07\%}$ at 1145 cm^{-1} by s-SNOM is shown in Fig. 3(c). (Broadband mid-IR spectra for the same locations were also identified in nano-FTIR [15].) Periodic high values in the relevant Gr layer are detected (white arrows), and the periodicity is in good agreement with the predicted value of about 400 nm. The Gr region is considered to have a high value of imaginary part of scattering coefficient, due to the coupling of Pt/Ir coated AFM probe and Gr layers. The enhancement of the absorption around Gr layers were also observed for the absorption distribution at other wave numbers at 1247 and 1269 cm^{-1} in Fig. 3(d) and Figs. S8 and S9 within the Supplemental Material [15,33–66].

Due to the strong coupling effect between the tip and the Gr, absolute distribution of absorption is always affected by the periodic Gr structure. Therefore, we focused on the three major absorption bands of 1145, 1247, and 1269 cm^{-1}, assigned as no dichroism, perpendicular dichroism, and parallel dichroism, respectively. To estimate the relative absorption to the isotropic band (1145 cm^{-1}), define $R_s = a_{1247,1269} - a_{1145}$. The s-SNOM image under the irradiation of QCL with varied wave numbers exhibit a drift in the imaging region; thus, the averaged line profile within ±200 nm around the Gr region was used to calculate R_s. Figure 3(d) shows the average R_s line profile around Gr, calculated from the absorption at 1145, 1247, and 1269 cm^{-1}. As shown in Fig. 3(d), the observed inhomogeneous distribution of the relative absorption suggests a systematic change of the PMMA absorption spectrum with increasing distance from Gr. Larger relative absorption of the parallel dichroic band at around the Gr region indicates that (i) PMMA chains are preferentially aligned in-plane near the Gr surface, and (ii) the orientation state differs between the central region of the PMMA and the Gr surface [illustrated in Figs. 3(e), and 3(f)]. This observation is consistent with microscale p-IR imaging results, which in far field show a generally orientation tendency of all the PMMA layers. The emergence of the subsurface layer induced by the Gr can also affect the in-plane thermal conductivity of the PMMA in the nanolaminates.

The anisotropic thermal conductivity for PMMA on a silica/silicon substrate is reported to be attributed to the alignment of polymer chains during viscous shearing in the spin coating [67]. However, in our case, the orientation in PMMA is unlikely induced by the fabrication process, since it involves a stress relief step (i.e., annealing at 150 °C for 5 min after drying in vacuum over) (see Fig. S1 within the Supplemental Material [15,33–62]). The positions of Raman G peak and 2D peak in the PMMA/Gr nanolaminates present minor differences as that of CVD Gr supported on Si/SiO_2 surface [68], which indicates Gr experiences a minor compression (approximately 0.08%) upon the fabrication process. Hence, such a compression cannot lead to an in-plane orientation of PMMA. Strikingly, a recent study [31] shows experimental evidence that Gr can induce an alignment of the EVA and PE chains through controllable solvent-polymer interactions. Thus, we infer that the Gr-induced PMMA orientation near the interface must be responsible for the anomalous $\kappa_{\parallel}$ (ϕ_{Gr}) and $\kappa_{\perp}$ (ϕ_{Gr}).

D. Modeling the thermal conductivity

We employed modified parallel and series models to represent the thermal conductivity in two directions. In these models, we introduced a term for the thermal conductivity of oriented PMMA layers, $\kappa_{PMMA,O}$, which includes both the highly oriented PMMA near the interface and a next outer layer, with thickness of $2R_g$, perturbed by the former according to simulation work [25]. The oriented PMMA chains are not flattened in a 2D plane or direction but at an oblique angle. As shown in Fig. 3(f), their spatial arrangement can influence both in-plane and cross-plane thermal conduction. Therefore, the parallel model can be

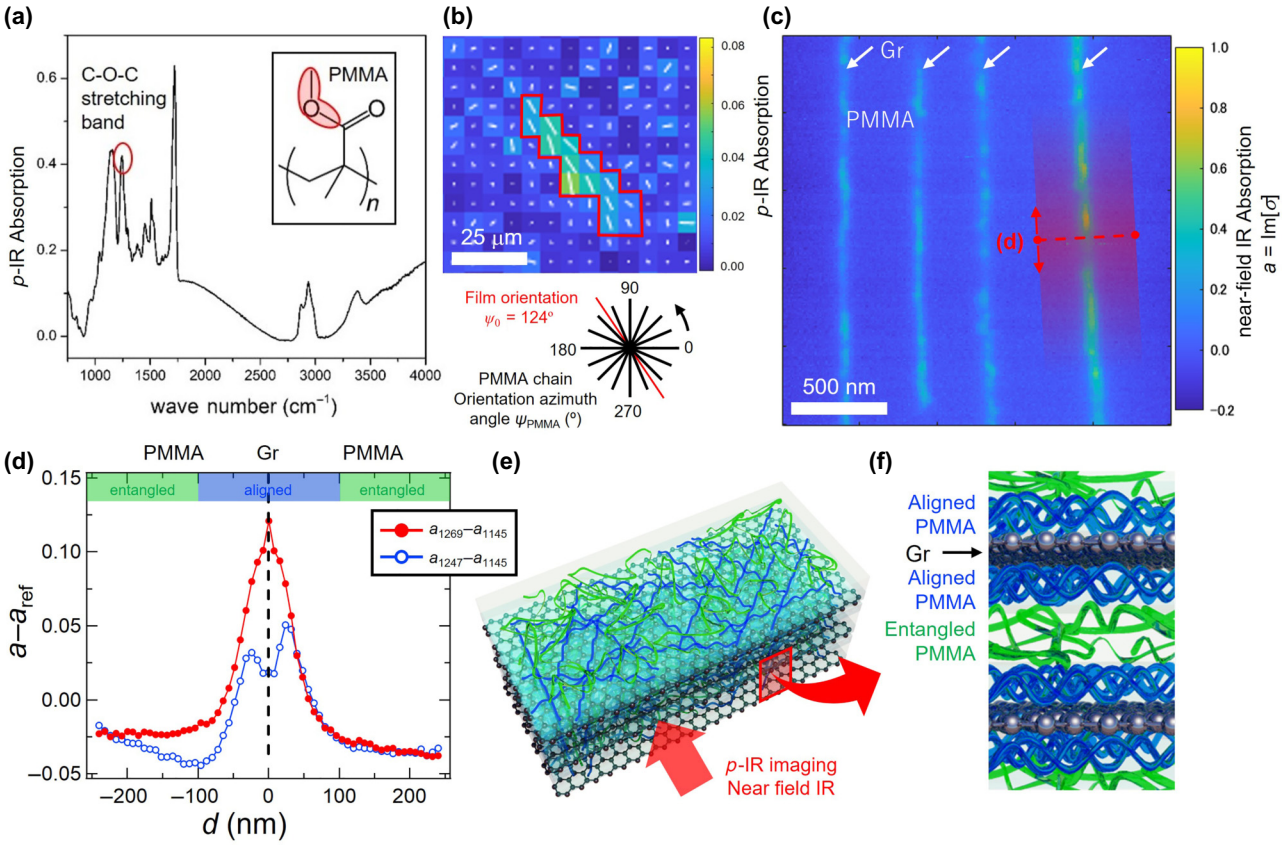

FIG. 3. Polymer planar orientation. (a) Exemplary p-IR absorption spectra of PMMA/$Gr_{1\%}$, displaying the C—O—C stretching band at 1242 cm^{-1}. Inset: the structural formula of PMMA where the C—O—C stretching band is highlighted in red. (b) Vector mapping of the macroscopic orientation azimuthal angle distribution at 1242 cm^{-1}. The background color image is the absorption distribution at 1242 cm^{-1}. White vectors indicate the direction of the orientation (ψ) while their lengths denote the degree of orientation according to color map of the p-IR absorption; $\psi = 0°$ is defined along the horizontal direction of the image. The pixels bordered with the red frame show the outline of the sample cross section of the investigated PMMA/$Gr_{1\%}$ film vertical to the paper face oriented along $\psi = 124°$. (c) The distribution of near field IR absorption $a = \mathrm{Im}[\sigma]$ of PMMA/$Gr_{0.07\%}$ nanolaminate measured by s-SNOM at C—O—C stretching band at 1145 cm^{-1}, where σ is the scattered electromagnetic field. (d) The averaged a–a_{ref} of the relative near-field IR absorption around a Gr layer represents the ratio of the perpendicular dichroic band (1247 cm^{-1}) and the paralleled dichroic band (1269 cm^{-1}) to the isotropic band (1145 cm^{-1}). The exemplary region of the average line profile is shown in (c) [(d) red area around the dashed line]. The shape variation of a–a_{ref} for the PMMA conformation sensitive band depends on the distance from the Gr layer. (e) Schematics of PMMA/Gr nanolaminate and the p-IR imaging. The red arrows indicate the direction of far-field p-IR and near-field IR measurement. (f) Schematics PMMA conformation distribution estimated from far-field orientation analysis and the near-field IR measurement.

rewritten as

$$\kappa_{\parallel}(\phi_{\mathrm{Gr}}) = (1 - \phi_{\mathrm{Gr}} - \phi_{\mathrm{PMMA,O}})\kappa_{\mathrm{PMMA}} + \phi_{\mathrm{Gr}}\kappa_{Gr,||} + \phi_{\mathrm{PMMA,O}}\kappa_{\mathrm{PMMA,O,||}} \quad (1)$$

where subscript PMMA,O,|| denotes oriented PMMA chains in the interface region assuming the thickness of $h_{\mathrm{PMMA,O}}$ with thermal conductivity, $\kappa_{\mathrm{PMMA,O,||}}$ parallel to the Gr layers. This thickness includes the oriented PMMA near the interface and a next outer layer with thickness of $2R_g$ perturbed by the former according to simulation work [25]. For the PMMA in the present experiment with molecular weight $M_w = 495$ kDa, the radius of gyration, $R_g \approx 17$ nm, is less than the thinner PMMA layer ($h_{\mathrm{PMMA}} = 34$ nm) in the present laminates. Hence for $h_{\mathrm{PMMA}} \geq 2h_{\mathrm{PMMA,O}}$, the fraction:

$$\phi_{\mathrm{PMMA,O}} = 2h_{\mathrm{PMMA,O}}/h_{\mathrm{PMMA}} = (2h_{\mathrm{PMMA,O}}/h_{\mathrm{Gr}})\phi_{\mathrm{Gr}} \quad (2)$$

where $h_{\mathrm{PMMA,O}} \approx 2R_g$ [24]. According to Fig. 2(a), $\kappa_{\parallel}(\phi_{\mathrm{Gr}})$ increases linearly with ϕ_{Gr} for $\phi_{\mathrm{Gr}} \leq 0.34\%$ with an intercept $\kappa_{\parallel} = \kappa_{\mathrm{PMMA}}$ ($=0.1 \mathrm{W m^{-1} K^{-1}}$) and a slope, $S \equiv \kappa_{\mathrm{Gr,||}} - \kappa_{\mathrm{PMMA}} + A(\kappa_{\mathrm{PMMA,O,||}} - \kappa_{\mathrm{PMMA}})$ ($=1320 \pm 76$)W m^{-1} K^{-1} with two unknown parameters ($\kappa_{\mathrm{Gr,||}}$, $\kappa_{\mathrm{PMMA,O,||}}$) assuming that $A \equiv 2h_{\mathrm{PMMA,O}}/h_{\mathrm{Gr}}$ ($\approx$200) is known. When ϕ_{Gr} exceeds approximately 0.5%, all PMMA layers with $h_{\mathrm{PMMA}} \leq 2h_{\mathrm{PMMA,O}} \approx 68$ nm, consist of oriented chains leading to $\phi_{\mathrm{PMMA,O}} = 1 - \phi_{\mathrm{Gr}}$. Hence,

$\kappa_{\parallel}(\phi_{Gr}) = \kappa_{PMMA,O,\parallel} + (\kappa_{Gr,\parallel} - \kappa_{PMMA,O,\parallel})\,\phi_{Gr}$ and now the intercept, and slope lead to $\kappa_{PMMA,O,\parallel} = 3.5$ W m^{-1} K^{-1}, and $\kappa_{Gr,\parallel} = 540$ W m^{-1} K^{-1}, respectively. Based on these two values, $S \simeq \kappa_{Gr,\parallel} + A\,\kappa_{PMMA,O,\parallel}$, which leads to either $A \simeq 229$ or to a higher $\kappa_{Gr,\parallel}$ (=640 W m^{-1} K^{-1}) mainly due to the uncertainty of the A value. In fact, the broad crossover [between the vertical dashed lines in Fig. 2(a)] falls between $\phi_{Gr} = 0.34\%$ and 0.56%. It therefore corresponds to an average $h_{PMMA} \approx 83$ nm or $h_{PMMA,O} \approx 2.4R_g$. i.e., roughly the chain end-to-end distance.

The Gr thermal conductivity $\kappa_{Gr,\parallel}$ can be strongly affected by the substrate, which results from ZA phonon scattering at the substrate boundary [21]. Earlier studies show that the supported monolayer Gr on a silicon dioxide substrate has a thermal conductivity of 600 Wm^{-1}K^{-1} [20,21], whose value can be further reduced to below 100Wm^{-1}K^{-1} in a sandwiched structure with Gr being encased between two silicon dioxide layers [69]. A residual polymeric layer can also reduce the thermal conductivity of a bilayer Gr to approximately 600 W m^{-1} K^{-1} [70]. Although different substrates cause varying degrees of scattering, the reported thermal conductivity of supported Gr has not exceeded 600 W m^{-1} K^{-1} [69,71]. Moreover, the grain boundaries in CVD Gr [72] and the present defects [D peaks in Fig. 1(b)] can further reduce thermal conductivity. Therefore, the estimated $\kappa_{Gr,\parallel} = 590 \pm 60$ W m^{-1} K^{-1} on both sides of the crossover composition [Fig. 2(a)] represents well the in-plane thermal conductivity of supported Gr.

In the cross-plane direction, the series model can now be rewritten as,

$$1/\kappa_{\perp} = \phi_{Gr}/\kappa_{Gr,\perp} + \phi_{PMMA,O}/(\kappa_{PMMA,O,\perp}) + (1 - 2\phi_{Gr} - \phi_{PMMA,O})/\kappa_{PMMA.} + \phi_{Gr}/(G_b h_{Gr}) \quad (3)$$

where $\kappa_{PMMA,O,\perp}$ is the cross-plane thermal conductivity of the PMMA, which is expected to be much lower than $\kappa_{PMMA,O,\parallel}$ but close to κ_{PMMA}. When $\phi_{Gr} \leq 0.34\%$, the linear representation of $1/\kappa_{\perp}$ with ϕ_{Gr} assumes the intercept $1/\kappa_{PMMA}$ and the slope $[1/\kappa_{Gr,\perp} + A/(\kappa_{PMMA,O,\perp}) + 1/(h_{Gr}G_b) - (A+2)/\kappa_{PMMA}]$ with two unknown parameters. Assuming $\kappa_{Gr,\perp} = 0.5$ W m^{-1} K^{-1} [73], $\kappa_{PMMA,O,\perp} = 0.17$ W m^{-1} K^{-1} is comparable with the bulk κ_{PMMA}. Above the crossover $\phi_{Gr} \geq 0.34\%$,

$$\kappa_{\perp} = \phi_{Gr}/\kappa_{Gr,\perp} + (1 - 2\phi_{Gr})/\kappa_{PMMA,O,\perp} + \phi_{Gr}/G_b/h_{Gr} \quad (4)$$

which captures within error the experimental $\kappa_{\perp}(\phi_{Gr} = 1\%)$ ($\sim$0.17 W m^{-1} K^{-1}) in Fig. 2(b) in support of the consistent representation of the cross-plane heat conductivity data. Notably the crossover $\phi_{Gr} \sim 0.4\%$ is found to be approximately the same for both $\kappa_{\parallel}$ (ϕ_{Gr}) and $\kappa_{\perp}(\phi_{Gr})$ in Fig. 2 suggesting a similar confinement effect of $\kappa_{PMMA,O}$ along both directions. Based on the two self-consistent models, the layer with predominantly oriented PMMA chains near the Gr-PMMA interface is about 35 times more thermally conductive than an amorphous bulk PMMA (=0.1Wm^{-1}K^{-1}). Thus, the modeling of the anisotropic heat conductivity of PMMA/Gr nanolaminates provides strong support of the presence of crossover behavior at a certain Gr loading.

III. RESULTS AND DISCUSSION

Previous results indicate that decreasing interfaces between filler and matrix reduces the total thermal resistance and weakens the phonon scattering [6]. Unprecedently, we found that the unmodulated Gr can align PMMA chains. Oriented polymers possess thermal conductivity of orders of magnitude higher than the bulk because of the restricted interchain hopping and the improved intrachain thermal transport [11,12,74,75]. We demonstrate that the PMMA chains near the interface show preferential in-plane orientation, which in turn enhances the thermal conductivity of the PMMA/Gr nanolaminates in both directions. This view diverges from conventional beliefs that interface in the nanocomposites can reduce thermal performance [5,6]. We infer that in previously studied randomly dispersed Gr nanocomposites, the nanostructure of the aligned PMMA is not fully taken advantage of, resulting in limited thermal conductivity enhancement.

It is worthwhile to note that the large graphene sheet may be crossed by bridges at regular intervals. It is possible that at same points the wrinkles of two neighboring graphene layers approaching each other with quite a thin layer of PMMA between them and lead to high electrical and heat conduction, due to the ballistic and tunneling effect. This picture is quite reasonable for electronic transport but may be a problem with thermal transport. Due to the lack of periodic lattice in amorphous polymers, atomic vibrations described by the phonon picture is always a settlement. The vibration modes in polymers are categories as propagons, diffusons, and locons, where diffusons are the main heat carriers [76]. Therefore, the phonons in graphene cannot tunnel through PMMA. However, recent works show that disordered materials can have a phonon-like mode, which can propagate hundreds of nanometers, supporting the phonon gas picture [77,78]. Although the measured thermal conductivity behavior in Fig. 2 cannot be fully captured by the "phonon bridge" picture, it is possible that the wrinkled graphene may contribute to the measured cross-plane thermal conductivity, which is worthy of further investigation.

In conclusion, exploiting the iterative "lift-off and float-on" wet transfer method to fabricate PMMA/Gr nanolaminates samples in even higher volume fractions has led to

the achievement of ultrahigh in-plane thermal conductivity and anisotropic conduction. The PMMA/Gr nanolaminates show a superhigh in-plane thermal conductivity of 8.9 W m^{-1} K^{-1} and high anisotropy of 53 at Gr loadings of 1 vol. %. The ultrahigh in-plane thermal conductivity is attributed to the perfect Gr alignment and increase of κ_{PMMA} in this direction, while the increase in cross-plane direction can be rationalized to the contribution of PMMA orientation. The results are key to understand the heat dissipation and thermal management mechanisms of Gr-based nanocomposites for their applications as TIMs.

ACKNOWLEDGMENTS

We are grateful to Ryohei Kikuchi (Institute of Science Tokyo, Research Infrastructure Management Center , Materials Analysis Division, Core Facility Center) for his help with microtome slices. C.G. and C.P. thank the financial support of "Graphene Core 3, GA: 881603 – Graphene-based disruptive technologies", which is implemented under the EU-Horizon 2020 Research & Innovation Action. X.X. would like to acknowledge the National Key R & D Project from Ministry of Science and Technology (China) (Grant No. 2024YFA1207900) and the National Natural Science Foundation of China (Grant No. 12174286). G.F. thanks the financial support by ERC AdG SmartPhon (Grant No. 694977). J.M. and M.R. thank the financial supports of JST CREST Grant (No. JPMJCR19I3), Japan, and an MEXT KAKENHI Grant (No. JP22H02137, JP23K23405). M.R thanks to partial support by MEXT KAKENHI Grant (No. JP22K14200).

DATA AVAILABILITY

The data that support the findings of this study are available from the corresponding author upon reasonable request.

[1] K. M. Shahil and A. A. Balandin, Graphene-multilayer graphene nanocomposites as highly efficient thermal interface materials, Nano Lett. **12**, 861 (2012).

[2] X. Xu, J. Chen, J. Zhou, and B. Li, Thermal conductivity of polymers and their nanocomposites, Adv. Mater. **30**, e1705544 (2018).

[3] S. E. Kim, F. Mujid, A. Rai, F. Eriksson, J. Suh, P. Poddar, A. Ray, C. Park, E. Fransson, Y. Zhong, D. A. Muller, P. Erhart, D. G. Cahill, and J. Park, Extremely anisotropic van der Waals thermal conductors, Nature **597**, 660 (2021).

[4] A. A. Balandin, S. Ghosh, W. Bao, I. Calizo, D. Teweldebrhan, F. Miao, and C. N. Lau, Superior thermal conductivity of single-layer graphene, Nano Lett. **8**, 902 (2008).

[5] C. Huang, X. Qian, and R. Yang, Thermal conductivity of polymers and polymer nanocomposites, Mater. Sci. Eng., R **132**, 1 (2018).

[6] X. Huang, C. Zhi, Y. Lin, H. Bao, G. Wu, P. Jiang, and Y.-W. Mai, Thermal conductivity of graphene-based polymer nanocomposites, Mater. Sci. Eng., R **142**, 100577 (2020).

[7] J. Chen, X. Xu, J. Zhou, and B. Li, Interfacial thermal resistance: Past, present, and future, Rev. Mod. Phys. **94**, 025002 (2022).

[8] E. T. Swartz and R. O. Pohl, Thermal boundary resistance, Rev. Mod. Phys. **61**, 605 (1989).

[9] M. Hu, P. Keblinski, and P. K. Schelling, Kapitza conductance of silicon–amorphous polyethylene interfaces by molecular dynamics simulations, Phys. Rev. B **79**, 104305 (2009).

[10] Z. Huang, C. Huang, D. Wu, and Z. Rao, Influence of chemical bonding on thermal contact resistance at silica interface: A molecular dynamics simulation, Comput. Mater. Sci. **149**, 316 (2018).

[11] S. Shen, A. Henry, J. Tong, R. Zheng, and G. Chen, Polyethylene nanofibres with very high thermal conductivities, Nat. Nanotechnol. **5**, 251 (2010).

[12] V. Singh, T. L. Bougher, A. Weathers, Y. Cai, K. Bi, M. T. Pettes, S. A. McMenamin, W. Lv, D. P. Resler, T. R. Gattuso, D. H. Altman, K. H. Sandhage, L. Shi, A. Henry, and B. A. Cola, High thermal conductivity of chain-oriented amorphous polythiophene, Nat. Nanotechnol. **9**, 384 (2014).

[13] L. Dong, Q. Xi, D. Chen, J. Guo, T. Nakayama, Y. Li, Z. Liang, J. Zhou, X. Xu, and B. Li, Dimensional crossover of heat conduction in amorphous polyimide nanofibers, Natl. Sci. Rev. **5**, 500 (2018).

[14] C. Pavlou, M. G. Pastore Carbone, A. C. Manikas, G. Trakakis, C. Koral, G. Papari, A. Andreone, and C. Galiotis, Effective EMI shielding behaviour of thin graphene/PMMA nanolaminates in the THz range, Nat. Commun. **12**, 4655 (2021).

[15] See Supplemental Material at http://link.aps.org/supplemental/10.1103/5zfl-986l for the interfacial thermal resistance, which includes Refs. [15,33–66].

[16] R. R. Nair, P. Blake, A. N. Grigorenko, K. S. Novoselov, T. J. Booth, T. Stauber, N. M. R. Peres, and A. K. Geim, Fine structure constant defines visual transparency of graphene, Science **320**, 1308 (2008).

[17] M. Kotsidi, G. Gorgolis, M. G. Pastore Carbone, G. Anagnostopoulos, G. Paterakis, G. Poggi, A. Manikas, G. Trakakis, P. Baglioni, and C. Galiotis, Preventing colour fading in artworks with graphene veils, Nat. Nanotechnol. **16**, 1004 (2021).

[18] B. Liu, C. Pavlou, Z. Wang, Y. Cang, C. Galiotis, and G. Fytas, Determination of the elastic moduli of CVD graphene by probing graphene/polymer Bragg stacks, 2D Mater. **8**, 035040 (2021).

[19] S.-I. Kim, J.-Y. Moon, S.-K. Hyeong, S. Ghods, J.-S. Kim, J.-H. Choi, D. S. Park, S. Bae, S. H. Cho, S.-K. Lee, and J.-H. Lee, Float-stacked graphene–PMMA laminate, Nat. Commun. **15**, 2172 (2024).

[20] W. Cai, A. L. Moore, Y. Zhu, X. Li, S. Chen, L. Shi, and R. S. Ruoff, Thermal transport in suspended and supported monolayer graphene grown by chemical vapor deposition, Nano Lett. **10**, 1645 (2010).

[21] J. H. Seol, I. Jo, A. L. Moore, L. Lindsay, Z. H. Aitken, M. T. Pettes, X. Li, Z. Yao, R. Huang, D. Broido, N. Mingo, R. S. Ruoff, and L. Shi, Two-dimensional phonon transport in supported graphene, Science **328**, 213 (2010).

[22] Y. Jin, C. Shao, J. Kieffer, M. L. Falk, and M. Shtein, Spatial nonuniformity in heat transport across hybrid material interfaces, Phys. Rev. B **90**, 054306 (2014).
[23] K. F. Mansfield and D. N. J. M. Theodorou, Atomistic simulation of a glassy polymer/graphite, Macromolecules **24**, 4295 (1991).
[24] A. N. Rissanou and V. Harmandaris, Structure and dynamics of poly(methyl methacrylate)/graphene systems through atomistic molecular dynamics simulations, J. Nanopart. Res. **15**, 1589 (2013).
[25] A. F. Behbahani, S. M. Vaez Allaei, G. H. Motlagh, H. Eslami, and V. A. Harmandaris, Structure, dynamics, and apparent glass transition of stereoregular poly(methyl methacrylate)/graphene interfaces through atomistic simulations, Macromolecules **51**, 7518 (2018).
[26] J. Zhou, Q. Xi, J. He, X. Xu, T. Nakayama, Y. Wang, and J. Liu, Thermal resistance network model for heat conduction of amorphous polymers, Phys. Rev. Mater. **4**, 015601 (2020).
[27] F. Huth, A. Govyadinov, S. Amarie, W. Nuansing, F. Keilmann, and R. Hillenbrand, Nano-FTIR absorption spectroscopy of molecular fingerprints at 20 nm spatial resolution, Nano Lett. **12**, 3973 (2012).
[28] T. Taubner, R. Hillenbrand, and F. Keilmann, Nanoscale polymer recognition by spectral signature in scattering infrared near-field microscopy, Appl. Phys. Lett. **85**, 5064 (2004).
[29] M. B. Raschke, L. Molina, T. Elsaesser, D. H. Kim, W. Knoll, and K. Hinrichs, Apertureless near-field vibrational imaging of block-copolymer nanostructures with ultrahigh spatial resolution, ChemPhysChem **6**, 2197 (2005).
[30] Y. Hikima, J. Morikawa, and T. Hashimoto, FT-IR image processing algorithms for in-plane orientation function and azimuth angle of uniaxially drawn polyethylene composite film, Macromolecules **44**, 3950 (2011).
[31] A. J. Carr, A. Head, J. A. Boscoboinik, S. R. Bhatia, and M. D. Eisaman, Direct evidence of graphene-induced molecular reorientation in polymer films, Adv. Mater. Interfaces **7**, 2000113 (2020).
[32] C. Valencia, C. H. Valencia, F. Zuluaga, M. E. Valencia, J. H. Mina, and C. D. Grande-Tovar, Synthesis and application of scaffolds of chitosan-graphene oxide by the freeze-drying method for tissue regeneration, Molecules **23**, 2651 (2018).
[33] J. Morikawa, T. Hashimoto, A. Kishi, Y. Shinoda, K. Ema, and H. Takezoe, Critical anomalies in thermal diffusivity of liquid-crystalline terephthal-bis-(4-*n*-butylaniline), Phys. Rev. E **87**, 022501 (2013).
[34] M. Ryu, J.-C. Batsale, and J. Morikawa, Quadrupole modelling of dual lock-in method for the simultaneous measurements of thermal diffusivity and thermal effusivity, Int. J. Heat Mass Transfer **162**, 120337 (2020).
[35] M. Ryu and J. Morikawa, Simultaneous measurements of anisotropic thermal diffusivity and thermal effusivity of liquid crystals using temperature wave analysis method, Jpn. J. Appl. Phys. **55**, 111701 (2016).
[36] Y. Hikima, J. Morikawa, and T. Hashimoto, Imaging of two-dimensional distribution of molecular orientation in poly(ethylene oxide) dpherulite using IR spectrum and birefringence, Macromolecules **45**, 8356 (2012).
[37] M. Ryu, A. Balčytis, X. Wang, J. Vongsvivut, Y. Hikima, J. Li, M. J. Tobin, S. Juodkazis, and J. Morikawa, Orientational mapping augmented sub-wavelength hyper-spectral imaging of silk, Sci. Rep. **7**, 7419 (2017).
[38] M. Ryu, R. Honda, A. Balčytis, J. Vongsvivut, M. J. Tobin, S. Juodkazis, and J. Morikawa, Hyperspectral mapping of anisotropy, Nanoscale Horiz. **4**, 1443 (2019).
[39] J. Dybal and S. Krimm, Normal-mode analysis of infrared and Raman spectra of crystalline isotactic poly (methyl methacrylate), Macromolecules **23**, 1301 (1990).
[40] A. National Institute of Advanced Industrial Science and Technology, SDBS No. 4062; and http://riodb01.ibase.aist.go.jp/sdbs/.
[41] B. H. Stuart, *Infrared Spectroscopy: Fundamentals and Applications* (John Wiley & Sons, 2004).
[42] J. You, H.-H. Choi, J. Cho, J. G. Son, M. Park, S.-S. Lee, and J. H. Park, Highly thermally conductive and mechanically robust polyamide/graphite nanoplatelet composites via mechanochemical bonding techniques with plasma treatment, Compos. Sci. Technol. **160**, 245 (2018).
[43] G. He, Z. Yang, X. Zhou, J. Zhang, L. Pan, and S. Liu, Polymer bonded explosives (PBXs) with reduced thermal stress and sensitivity by thermal conductivity enhancement with graphene nanoplatelets, Compos. Sci. Technol. **131**, 22 (2016).
[44] Z. Wu, C. Xu, C. Ma, Z. Liu, H. M. Cheng, and W. Ren, Synergistic effect of aligned graphene nanosheets in graphene foam for high-performance thermally conductive composites, Adv. Mater. **31**, 1900199 (2019).
[45] J.-N. Shi, M.-D. Ger, Y.-M. Liu, Y.-C. Fan, N.-T. Wen, C.-K. Lin, and N.-W. Pu, Improving the thermal conductivity and shape-stabilization of phase change materials using nanographite additives, Carbon **51**, 365 (2013).
[46] G. Li, X. Tian, X. Xu, C. Zhou, J. Wu, Q. Li, L. Zhang, F. Yang, and Y. Li, Fabrication of robust and highly thermally conductive nanofibrillated cellulose/graphite nanoplatelets composite papers, Compos. Sci. Technol. **138**, 179 (2017).
[47] A. Yu, P. Ramesh, M. E. Itkis, E. Bekyarova, and R. C. Haddon, Graphite nanoplatelet− epoxy composite thermal interface materials, J. Phys. Chem. C **111**, 7565 (2007).
[48] M. Shtein, R. Nadiv, M. Buzaglo, K. Kahil, and O. Regev, Thermally conductive graphene-polymer composites: size, percolation, and synergy effects, Chem. Mater. **27**, 2100 (2015).
[49] X. Zheng and B. Wen, Practical PBT/PC/GNP composites with anisotropic thermal conductivity, RSC Adv. **9**, 36316 (2019).
[50] Y.-j. Xiao, W.-y. Wang, X.-j. Chen, T. Lin, Y.-t. Zhang, J.-h. Yang, Y. Wang, and Z.-w. Zhou, Hybrid network structure and thermal conductive properties in poly (vinylidene fluoride) composites based on carbon nanotubes and graphene nanoplatelets, Composites, Part A **90**, 614 (2016).
[51] F. Luo, K. Wu, H. Guo, Q. Zhao, and M. Lu, Anisotropic thermal conductivity and flame retardancy of nanocomposite based on mesogenic epoxy and reduced graphene oxide bulk, Compos. Sci. Technol. **132**, 1 (2016).
[52] N. Song, D. Jiao, S. Cui, X. Hou, P. Ding, and L. Shi, Highly anisotropic thermal conductivity of layer-by-layer

assembled nanofibrillated cellulose/graphene nanosheets hybrid films for thermal management, ACS Appl. Mater. Interfaces **9**, 2924 (2017).

[53] Y. Guo, G. Xu, X. Yang, K. Ruan, T. Ma, Q. Zhang, J. Gu, Y. Wu, H. Liu, and Z. Guo, Significantly enhanced and precisely modeled thermal conductivity in polyimide nanocomposites with chemically modified graphene via in situ polymerization and electrospinning-hot press technology, J. Mater. Chem. C **6**, 3004 (2018).

[54] P. Kumar, S. Yu, F. Shahzad, S. M. Hong, Y.-H. Kim, and C. M. Koo, Ultrahigh electrically and thermally conductive self-aligned graphene/polymer composites using large-area reduced graphene oxides, Carbon **101**, 120 (2016).

[55] W. Yang, Z. Zhao, K. Wu, R. Huang, T. Liu, H. Jiang, F. Chen, and Q. Fu, Ultrathin flexible reduced graphene oxide/cellulose nanofiber composite films with strongly anisotropic thermal conductivity and efficient electromagnetic interference shielding, J. Mater. Chem. C **5**, 3748 (2017).

[56] J. Gong, Z. Liu, J. Yu, D. Dai, W. Dai, S. Du, C. Li, N. Jiang, Z. Zhan, and C.-T. Lin, Graphene woven fabric-reinforced polyimide films with enhanced and anisotropic thermal conductivity, Composites, Part A **87**, 290 (2016).

[57] H. Fang, Y. Zhao, Y. Zhang, Y. Ren, and S.-L. Bai, Three-dimensional graphene foam-filled elastomer composites with high thermal and mechanical properties, ACS Appl. Mater. Interfaces **9**, 26447 (2017).

[58] C.-P. Feng, L. Bai, Y. Shao, R.-Y. Bao, Z.-Y. Liu, M.-B. Yang, J. Chen, H.-Y. Ni, and W. Yang, A facile route to fabricate highly anisotropic thermally conductive elastomeric POE/NG composites for thermal management, Adv. Mater. Interfaces **5**, 1700946 (2018).

[59] J. S. Park, Y. J. An, K. Shin, J. H. Han, and C. S. Lee, Enhanced thermal conductivity of epoxy/three-dimensional carbon hybrid filler composites for effective heat dissipation, RSC Adv. **5**, 46989 (2015).

[60] Y. Zhuang, K. Zheng, X. Cao, Q. Fan, G. Ye, J. Lu, J. Zhang, and Y. Ma, Flexible graphene nanocomposites with simultaneous highly anisotropic thermal and electrical conductivities prepared by engineered graphene with flat morphology, ACS Nano **14**, 11733 (2020).

[61] H. Jung, S. Yu, N.-S. Bae, S. M. Cho, R. H. Kim, S. H. Cho, I. Hwang, B. Jeong, J. S. Ryu, J. Hwang, S. M. Hong, C. M. Koo, and C. Park, High through-plane thermal conduction of graphene nanoflake filled polymer composites melt-processed in an L-shape kinked tube, ACS Appl. Mater. Interfaces **7**, 15256 (2015).

[62] J. Zhang, W. Lei, D. Liu, and X. Wang, Synergistic influence from the hybridization of boron nitride and graphene oxide nanosheets on the thermal conductivity and mechanical properties of polymer nanocomposites, Compos. Sci. Technol. **151**, 252 (2017).

[63] M. Fujii, X. Zhang, H. Xie, H. Ago, K. Takahashi, T. Ikuta, H. Abe, and T. Shimizu, Measuring the thermal conductivity of a single carbon nanotube, Phys. Rev. Lett. **95**, 065502 (2005).

[64] X. Zhang, H. Q. Xie, M. Fujii, H. Ago, K. Takahashi, T. Ikuta, H. Abe, and T. Shimizu, Thermal and electrical properties of a suspended nanoscale thin film, Int. J. Thermophys. **28**, 33 (2006).

[65] B. Liu, J. Zhou, X. Xu, and B. Li, Thermal conductivity of one-dimensional organic nanowires: effect of mass difference phonon scattering, Nanotechnology **31**, 324003 (2020).

[66] J. Morikawa and T. Hashimoto, Thermal diffusivity of aromatic polyimide thin films by temperature wave analysis, J. Appl. Phys. **105**, 113506 (2009).

[67] S. Yamaguchi, T. Shiga, S. Ishioka, T. Saito, T. Kodama, and J. Shiomi, Anisotropic thermal conductivity measurement of organic thin film with bidirectional 3ω method, Rev. Sci. Instrum. **92**, 034902 (2021).

[68] C. Tsakonas, A. C. Manikas, M. Andersen, M. Dimitropoulos, K. Reuter, and C. Galiotis, In situ kinetic studies of CVD graphene growth by reflection spectroscopy, Chem. Eng. J. **421**, 129434 (2021).

[69] W. Jang, Z. Chen, W. Bao, C. N. Lau, and C. Dames, Thickness-dependent thermal conductivity of encased graphene and ultrathin graphite, Nano Lett. **10**, 3909 (2010).

[70] M. T. Pettes, I. Jo, Z. Yao, and L. Shi, Influence of polymeric residue on the thermal conductivity of suspended bilayer graphene, Nano Lett. **11**, 1195 (2011).

[71] J. Wang, L. Zhu, J. Chen, B. Li, and J. T. L. Thong, Suppressing thermal conductivity of suspended tri-layer graphene by gold deposition, Adv. Mater. **25**, 6884 (2013).

[72] W. Lee, K. D. Kihm, H. G. Kim, S. Shin, C. Lee, J. S. Park, S. Cheon, O. M. Kwon, G. Lim, and W. Lee, In-plane thermal conductivity of polycrystalline chemical vapor deposition graphene with controlled grain sizes, Nano Lett. **17**, 2361 (2017).

[73] Q. Fu, J. Yang, Y. Chen, D. Li, and D. Xu, Experimental evidence of very long intrinsic phonon mean free path along the c-axis of graphite, Appl. Phys. Lett. **106**, 031905 (2015).

[74] B. Li, F. DeAngelis, G. Chen, and A. Henry, The importance of localized modes spectral contribution to thermal conductivity in amorphous polymers, Commun. Phys. **5**, 323 (2022).

[75] Z. Cai, S. Lin, and C. Zhao, Anomalous diffuson and locon-dominated wigner multi-channel thermal transport in disordered and shear-aligned polymers, Macromolecules **57**, 6209 (2024).

[76] P. B. Allen, J. L. Feldman, J. Fabian, and F. Wooten, Diffusons, locons and propagons: Character of atomic vibrations in amorphous Si, Philos. Mag. B **79**, 1715 (1999).

[77] X. Liu, J. Feldman, D. Cahill, R. Crandall, N. Bernstein, D. Photiadis, M. Mehl, and D. Papaconstantopoulos, High thermal conductivity of a hydrogenated amorphous silicon film, Phys. Rev. Lett. **102**, 035901 (2009).

[78] K. T. Regner, D. P. Sellan, Z. Su, C. H. Amon, A. J. McGaughey, and J. A. Malen, Broadband phonon mean free path contributions to thermal conductivity measured using frequency domain thermoreflectance, Nat. Commun. **4**, 1640 (2013).